



Lithium iodide transport in double gyroid nanochannels formed by zwitterion-containing solid polymer electrolytes

Karim Aissou, Maximilien Coronas, Jason Richard, Camille Bakkali-Hassani, Sambhav Vishwakarma, Eddy Petit, Arie van Der Lee, Stéphanie Roualdès

► To cite this version:

Karim Aissou, Maximilien Coronas, Jason Richard, Camille Bakkali-Hassani, Sambhav Vishwakarma, et al.. Lithium iodide transport in double gyroid nanochannels formed by zwitterion-containing solid polymer electrolytes. *Journal of Polymer Science*, 2024, 62 (20), pp.4567-4575. 10.1002/pol.20240206 . hal-04772307

HAL Id: hal-04772307

<https://hal.science/hal-04772307v1>

Submitted on 8 Nov 2024

HAL is a multi-disciplinary open access archive for the deposit and dissemination of scientific research documents, whether they are published or not. The documents may come from teaching and research institutions in France or abroad, or from public or private research centers.


L'archive ouverte pluridisciplinaire **HAL**, est destinée au dépôt et à la diffusion de documents scientifiques de niveau recherche, publiés ou non, émanant des établissements d'enseignement et de recherche français ou étrangers, des laboratoires publics ou privés.



Distributed under a Creative Commons Attribution - NonCommercial 4.0 International License

RESEARCH ARTICLE

Lithium iodide transport in double gyroid nanochannels formed by zwitterion-containing solid polymer electrolytes

Karim Aissou¹  | Maximilien Coronas¹ | Jason Richard¹ |
Camille Bakkali-Hassani² | Sambhav Vishwakarma¹ | Eddy Petit¹ |
Arie van der Lee¹ | Stéphanie Roualdes¹

¹Institut Européen des Membranes, IEM, UMR 5635, Univ Montpellier, ENSCM, CNRS, Montpellier, France

²Institut Charles Gerhardt Montpellier, ICGM, UMR 5253, Univ Montpellier, ENSCM, CNRS, Montpellier, France

Correspondence

Karim Aissou, Institut Européen des Membranes, IEM, UMR 5635, Univ Montpellier, ENSCM, CNRS, Montpellier, France.

Email: karim.aissou@umontpellier.fr

Funding information

Agence Nationale de la Recherche, Grant/Award Number: ANR-18-CE09-00xx

Abstract

The fabrication of nanostructured block copolymer (BCP) films endowed with lithium ion-conducting gyroid (GYR) nanochannels is an appealing solution to build solid polymer electrolytes (SPEs) that combines high ionic conductivity (IC) with suitable mechanical properties. However, the formation of a well-developed GYR structure remains challenging to achieve from the self-assembly of polyelectrolyte BCP chains. To overcome this issue, large ion conducting gyroid grains were produced within freestanding polystyrene-*block*-poly(2-vinylpyridine)-*block*-poly(ethylene oxide) (PS-*b*-P2VP-*b*-PEO) films by combining a solvent vapor annealing (SVA) treatment with an infiltration process. Here, the SVA treatment enabled the manufacture of SPEs entirely composed of a GYR structure while the infiltration process allowed for the incorporation of an appropriate Li salt (i.e., lithium iodoacetate, LiIAC) within the 3D-interconnected nanochannels via a Menshutkin reaction. By using this SVA-Infiltration strategy, it has been demonstrated that the creation of ion conducting GYR nanochannels enhances the ion transportation capacity of pyridine-containing SPEs since substantially lower ICs were measured from analog PS-*b*-P2VP-*b*-PEO/LiIAC films having a nominally disordered as-cast state. Remarkably, zwitterionic pyridinium-based moieties formed inside the interpenetrated nanochannels enable an efficient migration of Li⁺ and I₃[−] species, leading to an IC as high as 10^{−4} S cm^{−1} at 70°C.

KEYWORDS

block copolymer electrolyte, double-gyroid, ionic conductivity, self-assembly, solvent vapor annealing

1 | INTRODUCTION

Among the various alternative energies employed to accelerate the transition toward a world with carbon-free mobility, lithium-ion batteries (LIBs) have emerged as

one of the dominant energy storage solutions to replace conventional fossil fuels that power vehicle engines.^{1–3}

However, to supplant effectively the diesel and petrol cars, LIBs endowed with better performances (i.e., higher-energy density and lower electrochemical potential) are

This is an open access article under the terms of the [Creative Commons Attribution-NonCommercial](https://creativecommons.org/licenses/by-nc/4.0/) License, which permits use, distribution and reproduction in any medium, provided the original work is properly cited and is not used for commercial purposes.

© 2024 The Author(s). *Journal of Polymer Science* published by Wiley Periodicals LLC.

urgently needed in order to improve the electric vehicle ranges.⁴ To make progress in the race to achieve better performances, one promising approach relies on the use of Li metal as ultimate anode (theoretical capacity of 3860 mAh g⁻¹) to replace the graphite electrode.^{5,6} However, during the repeated Li stripping/plating process, the lithium metal suffers from safety issues (e.g., thermal instability and flammability) due to the destruction of the solid electrolyte interface (SEI) and the formation of lithium dendrites that can penetrate the separator, and eventually create internal short-circuits.⁷ To address this safety concern, solid polymer electrolytes (SPEs) have attracted great attention to replace the conventional liquid electrolyte since SPEs, made of a mixture of homopolymer⁸ or block copolymer^{9,10} (BCP) chains and Li salts, have the potential to suppress efficiently the Li dendrite formation in Li-metal batteries, particularly if a lithium iodide additive is used.^{11,12}

For practical use, SPEs also have to meet minimum battery conductivity requirements of 10⁻⁴ S cm⁻¹. To achieve this high ionic conductivity (IC) while preventing the Li-dendrite formation, an ideal SPE architecture offering a strong decoupling between the conductive and mechanical properties is highly desired.^{13,14} This attractive SPE architecture could be reached by creating ion conductive nanochannels, with continuous and uninterrupted pathways, integrated inside an insulating polymer matrix having suitable mechanical properties. An appealing approach to manufacture such nanostructured SPEs is to produce a gyroid (GYR) morphology with ion conducting pathways by using self-assembled ionic aggregate^{15,16} or BCP¹⁷⁻¹⁹ templates since the GYR phase can transport ions through all three directions, which obviates the need for channel alignment.

Besides, to optimize the overall IC and suppress the Li-dendrite growth, zwitterion (ZI)-based electrolytes have emerged as interested materials since a thinner SEI, a higher columbic efficiency as well as an improved IC can be reached by adding ZI in the electrolyte formulation.²⁰⁻²² Following this paradigm shift, the Segalman group has recently demonstrated an unprecedented lithium ion-conductivity (1.6 mS cm⁻¹) and selectivity ($t_+ \approx 0.6-0.8$) by using blends of polymerized zwitterionic liquids (PZILs) and Li salts as new design platforms for SPEs.²³

Herein, a novel zwitterion-containing solid polymer electrolyte (ZI-SPE) endowed with interconnected ion conductive nanochannels was manufactured via a two-step method. For that purpose, 25 μ m thick polystyrene-*block*-poly(2-vinylpyridine)-*block*-poly(ethylene oxide) (PS-*b*-P2VP-*b*-PEO) films entirely composed of a GYR structure were first generated by using a solvent vapor annealing (SVA) treatment. These GYR-forming terpolymer films were then infused by a lithium iodoacetate (LiIAC) solution for 48 h to transform the pyridine sites into zwitterionic 2-(pyridinium-1yl)acetate moieties via

a Menshutkin reaction. Interestingly, an IC as high as 1.9×10^{-5} S cm⁻¹ was measured at 60°C from GYR-structured SPEs generated by SVA when the infiltration process was carried out for 1 h. This value was found to be an order of magnitude higher than that measured from as-cast SPEs, consisting of a thick (~ 25 μ m) substructure having a disordered (DIS) phase and a thin (~ 200 nm) skin layer exhibiting out-of-plane ion conducting lamellae (1.5×10^{-6} S cm⁻¹ at 60°C). Here, the overall IC of GYR-forming SPEs was limited to the single Li-ion conduction because charge-transfer complexes between LiIAC and pyridine nitrogen atoms, immobilizing the acetate counter-ion, were formed during short infiltration process durations. Conversely, ZI-SPEs, with gyroid conductive nanochannels exhibiting ICs $>10^{-4}$ S cm⁻¹ above 70°C, were produced when the infiltration process was carried out for 48 h due to the formation of pyridinium centers that enable the fabrication of dual-ion (Li⁺ and I₃⁻) conducting electrolytes. For this infiltration duration, the GYR-forming PS-*b*-P2VP-*b*-PEO film also has a higher ion conductivity than that probed from an analog SPE having a substructure with a DIS phase (1.1×10^{-5} S cm⁻¹ at 70°C).

2 | RESULTS

The linear ABC triblock terpolymer used in this work consists of PS (45 kg mol⁻¹, $\phi_{PS} \sim 0.65$), P2VP (16 kg mol⁻¹, $\phi_{P2VP} \sim 0.22$) and PEO (8.5 kg mol⁻¹, $\phi_{PEO} \sim 0.13$), where ϕ is the volume fraction of the corresponding block. Figure 1 illustrates the process route used to produce a freestanding GYR-forming ZI-SPE endowed with dual-ion conductive nanochannels. To this end, a 25 μ m thick PS-*b*-P2VP-*b*-PEO film, casted on a (3 \times 3 cm) silicon substrate with sacrificial water-soluble layer, was first solvent-annealed [15 h, dichloromethane (DCM)] to achieve the GYR structure. After detaching the terpolymer film from its substrate by solubilizing the sacrificial layer in a water bath, the freestanding PS-*b*-P2VP-*b*-PEO layer shaped into a 2.5 cm diameter disc was then reacted with a 1 wt% of LiIAC solution to form 2-(pyridinium-1yl)acetate on the 2VP moieties as shown on the schematic reaction diagram. Note that charge-transfer complexes between LiIAC and reactive pyridine nitrogen atoms [noted (1)] are mainly formed after 1 h of reaction at 30°C while cationic pyridinium centers with iodides as counter-ions [noted (2)] are also observed when the reaction is carried out for 48 h (see the discussion hereafter).

Figure 2 shows atomic force microscopy (AFM) topographic images of a PS-*b*-P2VP-*b*-PEO film before and after the SVA treatment. The as-cast PS-*b*-P2VP-*b*-PEO layer, generated by using a tape casting technique, exhibits a top surface with a lamellar (LAM) morphology that locally resembles to a perforated lamellar (PL) structure

FIGURE 1 Schematic overview of the SVA-Infiltration process route used to produce freestanding GYR-forming ZI-SPEs endowed with dual-ion conductive nanochannels. (1) and (2) represent the charge-transfer complexes between P2VP and LiIAc (green) and the formation of 2-(pyridinium-1-yl)acetate, respectively. GYR, gyroid; SVA, solvent vapor annealing; ZI-SPEs, zwitterion-containing solid polymer electrolytes.

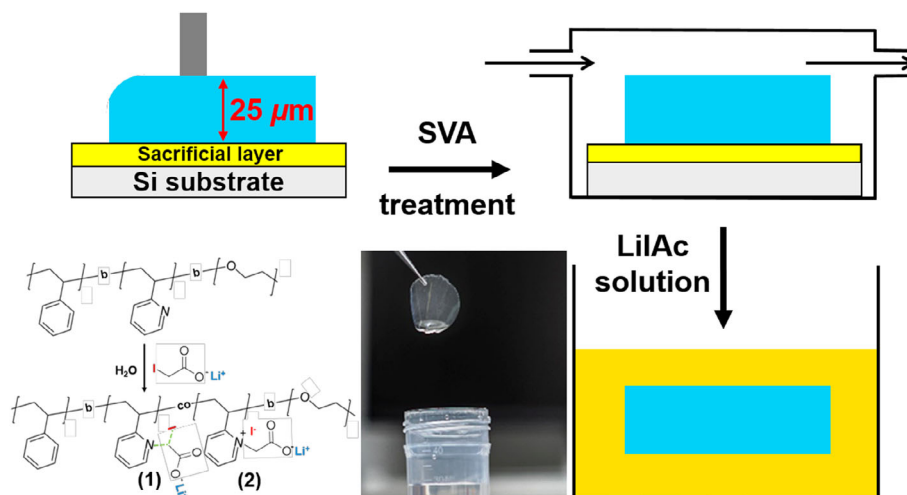
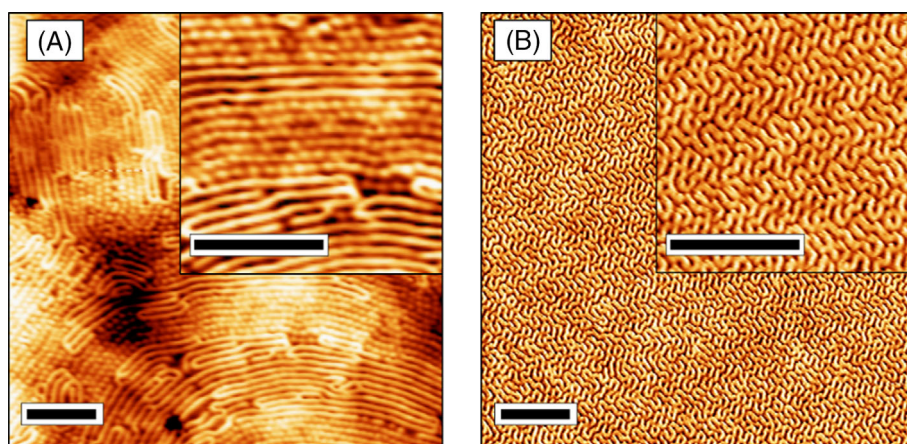


FIGURE 2 ($3 \times 3 \mu\text{m}$ and magnified $1 \times 1 \mu\text{m}$) AFM topographic images of a PS-*b*-P2VP-*b*-PEO layer acquired (A) before and (B) after the SVA treatment where the PS matrix and P2VP/PEO nanochannels appear in bright and dark, respectively. The as-cast PS-*b*-P2VP-*b*-PEO film exhibits a PL-like morphology that is transformed into a highly-ordered GYR structure after exposition to a DCM vapor for 15 h. Scale bars: 500 nm. AFM, atomic force microscopy; GYR, gyroid; PL, perforated lamellar; SVA, solvent vapor annealing.



with (bright) PS perforations having a period of ~ 48 nm (see Figure 2A).²⁴ In contrast, a highly-ordered gyroid structure is produced on the top surface of a PS-*b*-P2VP-*b*-PEO film exposed to a DCM vapor for 15 h (see Figures 2B and S1).

The cross-section scanning electron microscopy (SEM) image presented in Figure S2a shows that a 25 μm thick PS-*b*-P2VP-*b*-PEO film having a DIS state (i.e., no-evidence of nanochannels formation within its substructure) is produced after the casting process. Indeed, the magnified SEM view taken in the vicinity of the top surface revealed that the LAM structure formed on the as-cast PS-*b*-P2VP-*b*-PEO material (see Figure 2A) did not propagate deeply within the material ($\text{LAM}_{\text{thickness}} \approx 200$ nm) during the casting process (see Figure S2b). Note that a dense bottom layer is also formed at the opposite interface of the as-cast PS-*b*-P2VP-*b*-PEO layer (see Figure S2c). The presence of a nominally disordered (as-cast) state within the substructure is also confirmed by the grazing incidence small-angle X-ray scattering (GISAXS) data since a diffuse scattering pattern, arising from the lack of order through the entire film thickness, can be observed (see Figure S3a). Conversely, a well-

developed GYR structure is produced within the entire terpolymer film thickness after the SVA treatment as shown on the cross-section SEM images presented in Figure 3. Here, large gyroid grains are formed in the vicinity of the top and bottom surfaces as well as in the middle of the 25 μm thick PS-*b*-P2VP-*b*-PEO film generated by SVA (15 h, DCM). GISAXS data presented in Figure S3b confirm the formation of a well-developed GYR structure at large scale since multiple sharp peaks can be clearly observed from the scattering pattern.

To prepare ion conductive electrolytes, the freestanding PS-*b*-P2VP-*b*-PEO films generated by SVA were infused by a 1 wt% of LiIAc solution maintained at 30°C for different times. Figure 4A displays the Fourier-transform infrared (FTIR) traces for the GYR-forming film before and after reaction with LiIAc in the range of 1500–1750 cm^{-1} . In addition to the C–N stretching vibration mode of the free P2VP band occurring at 1590 cm^{-1} , a new vibrational peak is observed at 1600 cm^{-1} when the GYR-forming film was infiltrated for 1 h. This variation is attributed to the constraint on the free rotation of pyridine ring resulting from (partial) interactions between some

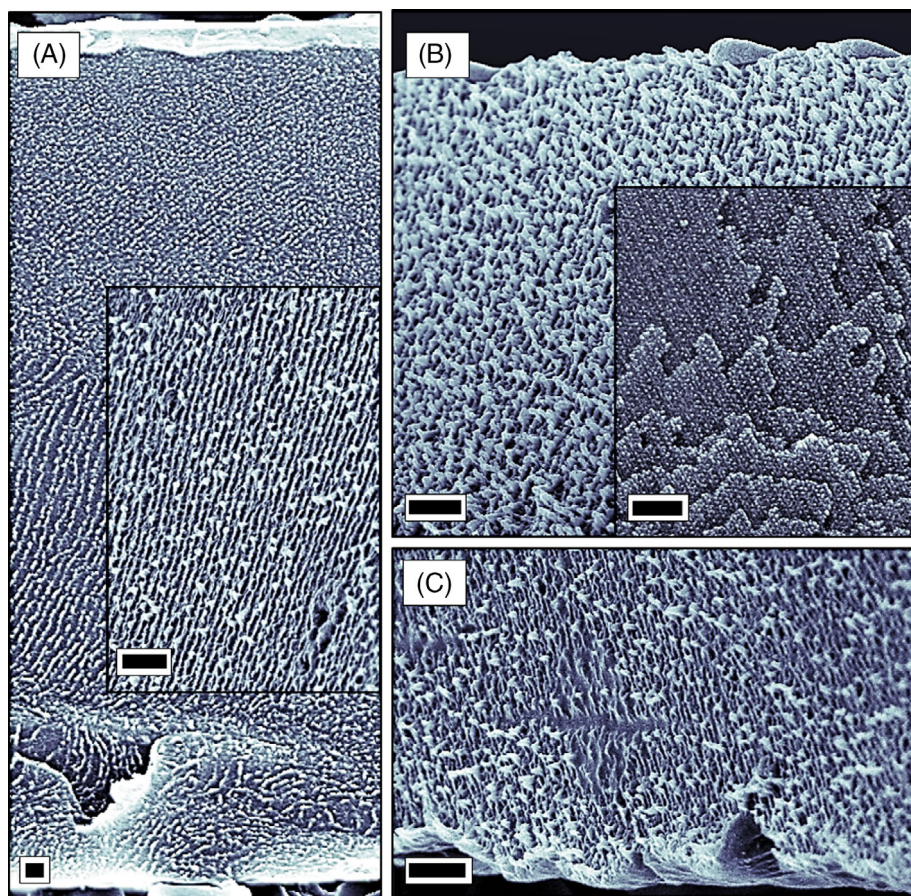


FIGURE 3 Cross-sectional SEM views of a 25 μm thick PS-*b*-P2VP-*b*-PEO layer generated by SVA (15 h, DCM) showing (A) the presence of large gyroid grains within the entire film thickness and details of the GYR structure in the vicinity of the (B) top and (C) bottom film regions. Insets (A) and (B) show a stack of gyroid planes and the pattern (i.e., nanochannels arrangement) formed in these planes, respectively. Scale bars: 500 nm. GYR, gyroid; SEM, scanning electron microscopy; SVA, solvent vapor annealing.

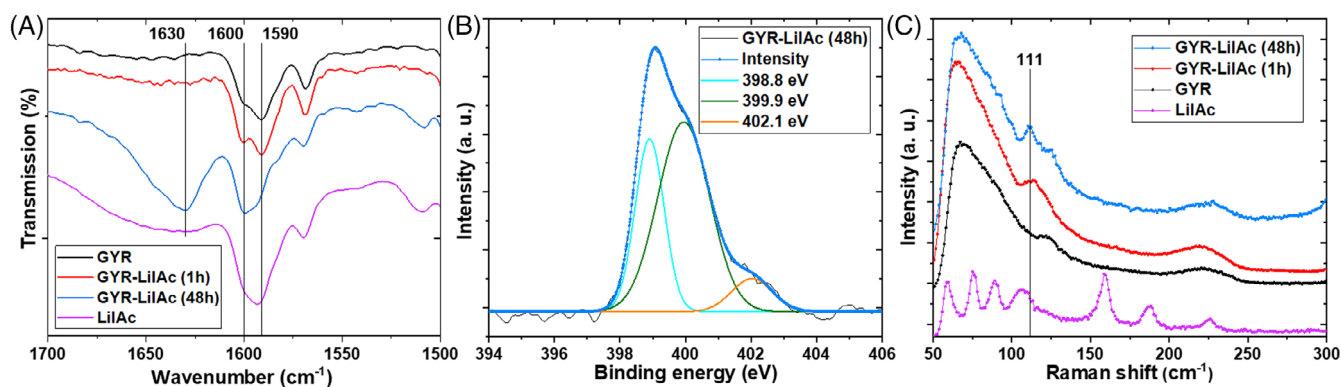


FIGURE 4 (A) FTIR spectra of GYR-forming films infused by a LiIAc solution for different times: (black) no-treatment, (red) 1 h and (blue) 48 h. The new bands at 1600 and 1630 cm^{-1} attest for the formation of charge-transfer complexes and pyridinium sites, respectively. The (pink) FTIR spectrum of the LiIAc powder is given for comparison. (B) N1s XPS spectrum of an infiltrated (48 h) PS-*b*-P2VP-*b*-PEO layer showing the formation of (green) charge-transfer complexes and (orange) pyridinium sites at 399.9 and 402.1 eV, respectively. (C) Raman spectra of GYR-structured films infused by a LiIAc solution for different times: (black) no-treatment, (red) 1 h and (blue) 48 h. The formation of I_3^- species is revealed by the presence of its characteristic band at 111 cm^{-1} . The (pink) Raman spectrum of the LiIAc powder is also shown for comparison. FTIR, Fourier-transform infrared; GYR, gyroid; XPS, X-ray photoelectron spectroscopy.

pyridine nitrogen atoms and LiIAc. After an infiltration duration of 48 h, the number of interactions between pyridine nitrogen atoms and LiIAc is observed to increase since the free P2VP band at 1590 cm^{-1} has mainly shifted to 1600 cm^{-1} . For such infiltration conditions, the

formation of zwitterionic moieties is evidenced by the apparition of the C-N⁺ stretching vibration mode of pyridinium at 1630 cm^{-1} ,²⁵ which was not observed after only 1 h of reaction. Note that the existence of two type of associations has been monitored by FTIR during the reaction of R-

and S-mandelic acids with P2VP: one is corresponding to hydrogen bonding between dopant and pyridine (1600 cm^{-1}) and the other is resulting from protonated nitrogen on the pyridine (1620 cm^{-1}).²⁶ The presence of pyridinium sites was also confirmed by X-ray photoelectron spectroscopy (XPS) since a peak fraction of the N1s core level shifted of $\sim 3.2\text{ eV}$ (402.1 eV) after reaction with LiIAC for 48 h (see Figure 4B).^{27,28} Although, no change was observed on the N1s XPS data before and after reaction with LiIAC for 1 h (see Figure S4), I3d XPS spectra confirmed that charge-transfer complexes between LiIAC and reactive pyridine nitrogen atoms occurred in the infiltrated (1 h) PS-*b*-P2VP-*b*-PEO layer since both the I3d_{3/2} (620.1 eV) and I3d_{5/2} (631.6 eV) peaks of pure LiIAC have been shifted of $\sim 2\text{ eV}$ (see Figure S5). Note that XPS data for the infiltrated (48 h) PS-*b*-P2VP-*b*-PEO film indicate that an excess (i.e., unreacted) of LiIAC molecules is adsorbed in the sample since two binding energies (BEs) are observed for the I3d_{3/2} (620.3 and 618.2 eV) and I3d_{5/2} (632.1 and 629.7 eV) peaks. As this excess of LiIAC salt is observed for both the as-cast and GYR-structured PS-*b*-P2VP-*b*-PEO films infiltrated for 48 h, it will lead to an overestimation of their intrinsic IC properties but will not alter the conclusion regarding the effect of creating 3D-interconnected nanochannels to enhance the ion transport within SPEs (see discussion below). The presence of iodide species was established by the

Raman analyses, as presented on the obtained spectra in Figure 4C. Indeed, a weak band at 111 cm^{-1} , assigned to the symmetrical stretching mode of I_3^- species,^{29–31} is observed in the GYR-forming film infused by a LiIAC solution for 1 h. This (111 cm^{-1}) band is much stronger in the Raman spectrum of the PS-*b*-P2VP-*b*-PEO layer generated by SVA-Infiltration (48 h), confirming the release of iodide species by the reaction of LiIAC with the P2VP moieties.

To determine the mode of ion transport within the GYR-structured ZI-SPEs generated by SVA-Infiltration, electrochemical impedance spectroscopy (EIS) measurements were conducted at different temperatures between two gold-plated blocking electrodes in a through-plane configuration cell. Prior to EIS measurements, the GYR-forming ZI-SPE sample was heated at 50°C for 1 h and, subsequently, equilibrated at 20°C to eliminate traces of water and to ensure a good interfacial contact with the electrodes. Figure 5A shows the Nyquist plot of an infiltrated (48 h) PS-*b*-P2VP-*b*-PEO film measured at 20, 40, 65, and 90°C . Plots established at low temperatures revealed that the IC is ruled by intra-grain (GYR nanochannels) and inter-grain (grain boundary, GB) contributions since two partly formed semicircles as well as a capacitive tail can be observed on curves.³² This behavior, fully-supported by the architecture of solvent-annealed (15 h, DCM) PS-*b*-P2VP-*b*-PEO films exhibiting large gyroid grains (see Figure 3), has been previously observed

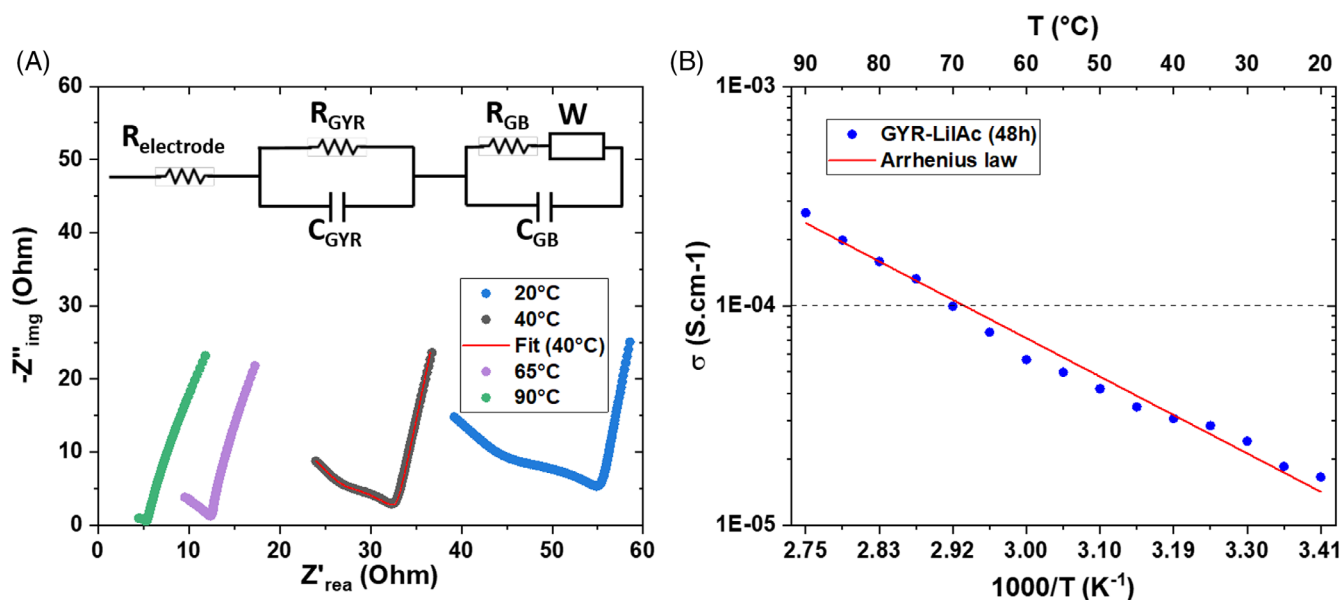


FIGURE 5 (A) Nyquist plot of an infiltrated (48 h) PS-*b*-P2VP-*b*-PEO film recorded at different temperatures: (blue) 20°C , (black) 40°C , (purple) 65°C , and (green) 90°C . The total IC of the GYR-structured ZI-SPE sample is fitted by using an equivalent circuit model that separates the intra-grain (GYR) and inter-grain (GB) contributions (see red fitting curve at 40°C). (B) Arrhenius plot of IC versus inverse temperature determined by EIS in the range of 20 – 90°C for an infiltrated (48 h) GYR-forming SPE. EIS, electrochemical impedance spectroscopy; GYR, gyroid; IC, ionic conductivity; ZI-SPE, zwitterion-containing solid polymer electrolyte.

from GYR-structured hybrid electrolytes endowed with ceramic and polymer microchannels.³³ As illustrated for the curve acquired at 40°C, experimental data are well-fitted by an equivalent circuit model comprising a Warburg (W) element that represents the blocked-diffusion of ions, an electrode resistance ($R_{\text{electrode}}$) and two parallel arrangements of a resistor (R_{GYR} and R_{GB}) and a capacitance (C_{GYR} and C_{GB}) (see red plot). Note that the GB contribution, corresponding to the low-frequency semicircle,³² decreases more rapidly with temperature than that arising from the intra-grain ion transport to vanish above 65°C (see purple dotted curve). The temperature-dependent IC of a 25 μm thick GYR-structured ZI-SPE is presented in Figure 5B. Data recorded between 20 and 90°C show that the IC (σ) value exceeds $10^{-4} \text{ S cm}^{-1}$ at 70°C, and are better fitted using the Arrhenius law instead of the Vogel-Tamman-Fulcher (VTF) equation, which indicates that ion transport essentially occurs through a hopping mechanism.³⁴

Note that a lower IC value ($1.1 \times 10^{-5} \text{ S cm}^{-1}$) was measured at 70°C from an as-cast PS-*b*-P2VP-*b*-PEO SPE infused by a LiIAC solution for 48 h which indicates that the presence of 3D interconnected nanochannels within the entire film thickness is attractive to improve the ion transport within the SPE (see Figure S6). To further investigate this phenomenon, the IC values were also measured from as-cast and GYR-structured SPEs infused

by a LiIAC solution for 1 h (see Figure 6). As the as-cast PS-*b*-P2VP-*b*-PEO film architecture consists mainly of a DIS phase, it will be used as reference to determine how much the ion conductivity is affected by the creation of 3D interconnected pathways within the entire SPE thickness. The Nyquist plot recorded at 60°C for a GYR-structured SPE infused by a LiIAC solution for 1 h confirms that the total IC could be divided into two contributions attributed to the GYR and GB ion transport (see Figure 6A inset). In contrast, data acquired in similar conditions from the DIS phase shows solely the formation of a semicircle and a capacitive tail due to the absence of GBs. From these results, an IC as high as $1.9 \times 10^{-5} \text{ S cm}^{-1}$ was measured at 60°C from the GYR-forming SPE which revealed to be an order of magnitude higher than that measured from the as-cast material ($1.5 \times 10^{-6} \text{ S cm}^{-1}$ at 60°C). The temperature-dependent IC plots of as-cast and solvent-annealed PS-*b*-P2VP-*b*-PEO SPEs infused by a LiIAC solution for 1 h evidence that the creation of ion conducting nanochannels with physical continuity through the entire film thickness is benefit to optimize the ion transport since the σ_{GYR} values are significantly higher than that probed in the DIS phase in the range of 30–70°C (see Figure 6B).

Interestingly, a nonlinear VTF and linear Arrhenius model was used to fit the data measured from the as-cast and solvent-annealed PS-*b*-P2VP-*b*-PEO SPEs, respectively,

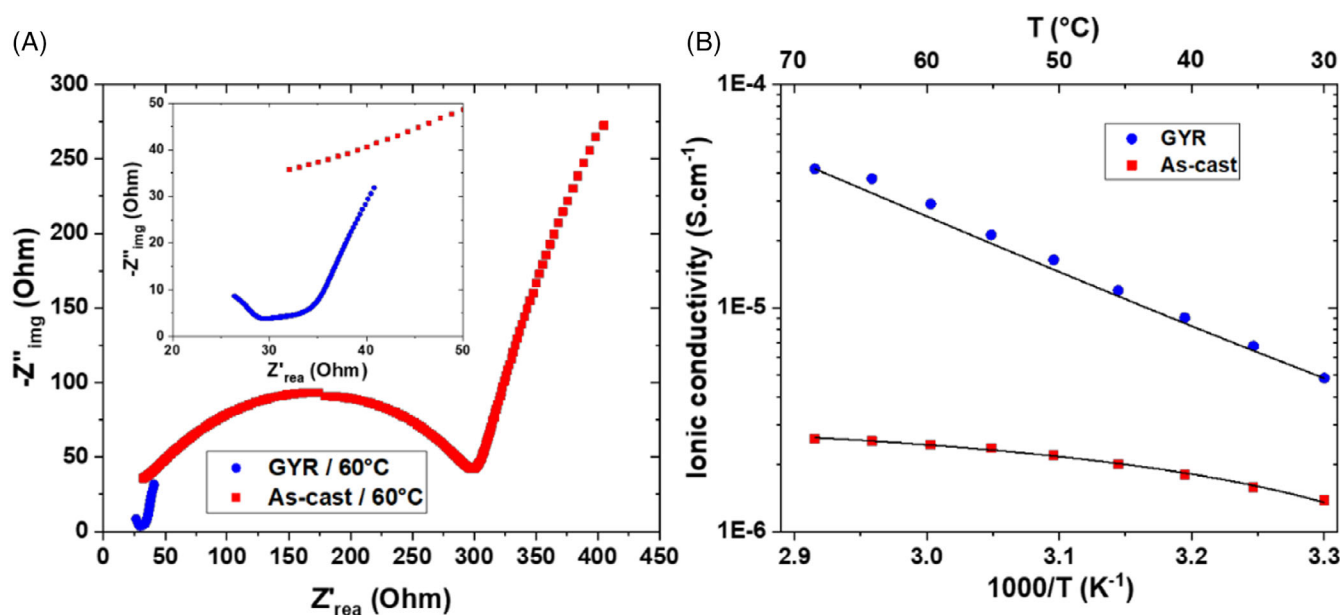


FIGURE 6 (A) Nyquist plot of infiltrated (1 h) PS-*b*-P2VP-*b*-PEO SPEs endowed with a (blue) GYR or (red) DIS (as-cast) phase. Data recorded at 60°C clearly evidence that the ion transport is faster for the blue dotted curve exhibiting two partly formed semicircles due to the formation of GBs within the GYR phase (see inset). (B) Plot of IC versus inverse temperature determined by EIS in the range of 30–70°C for infiltrated (1 h) SPEs with a (blue) GYR or (red) DIS (as-cast) phase. A nonlinear and linear model was used to fit the data measured before and after the SVA treatment (15 h, DCM), respectively. DIS, disordered; EIS, electrochemical impedance spectroscopy; GYR, gyroid; IC, ionic conductivity; SVA, solvent vapor annealing; SPE, solid polymer electrolyte.

which reveals that the ion diffusion operates via two different mechanisms within the GYR and DIS phases.

The mechanical properties of the 25 μm thick GYR structured film were evaluated by dynamic mechanical analysis (DMA) over the temperature range 25–200°C. The data presented in Figure S7 show that a higher storage modulus, E' , is observed for the PS-*b*-P2VP-*b*-PEO film in the temperature range of 25–70°C. Above 70°C, the E' values decrease progressively, which may be due to the glass transition temperature of polystyrene, $T_{\text{g,PS}}$, that we have previously measured at 89°C by differential scanning calorimetry (DSC) from the terpolymer powder.²⁴ For this PS-*b*-P2VP-*b*-PEO film, a plateau was also observed between 110 and 200°C, and would correspond to a stabilization of the mechanical properties of the GYR structure above $T_{\text{g,PS}}$. The associated image shows that the 25 μm thick PS-*b*-P2VP-*b*-PEO film did not break under stress at 200°C.

3 | CONCLUSION

We present a strategy to manufacture GYR-structured SPEs endowed with 3D-interconnected ion conductive nanochannels. This architecture generated by SVA-Infiltration allows to optimize the overall ion conductivity of the terpolymer material over a wide temperature range since the ion transport within GYR nanochannels is always well-above than that measured within the DIS (as-cast) phase. For instance, our results reveal that the manufacture of ZI-SPEs composed entirely of a GYR morphology enables to achieve an IC as high as $10^{-4} \text{ S cm}^{-1}$ at 70°C. In contrast, a lower IC value of $\sim 1.1 \times 10^{-5} \text{ S cm}^{-1}$ was probed at 70°C from an analog terpolymer film having a disordered phase.

4 | EXPERIMENTAL

4.1 | Material

1,4-dioxane (DOX, 99.5%), tetrahydrofuran (THF, 99%), DCM (99%), LiIAC (>97%) and poly(3,4-ethylenedioxythiophene): polystyrene sulfonate (PEDOT:PSS, 2.8 wt% in water) were purchased from Sigma Aldrich. Silicon substrates were provided from silicon materials (Si-Mat). PS-*b*-P2VP-*b*-PEO (S : V : EO \approx 65 : 22 : 13, 69.5 kg mol^{-1}) was purchased from Polymer Source inc (Canada).

4.2 | Fabrication of DIS and GYR-structured PS-*b*-P2VP-*b*-PEO films

The 25 μm thick PS-*b*-P2VP-*b*-PEO films having a substructure with a nominally disordered state were casted

from a 20 wt% terpolymer solution in a di-solvent mixture (DOX/THF: 70/30 by weight) onto ($3 \times 3 \text{ cm}$) silicon substrates, covered by a sacrificial PEDOT:PSS layer, by using a tape casting technique with a 400 μm blade. To manufacture PS-*b*-P2VP-*b*-PEO films entirely composed of a DG structure, the terpolymer materials were exposed to a DCM vapor for 15 h in order to promote the mobility of BCP chains until reaching the formation of the DG structure. Here, a continuous flow system was used to control the DCM vapor pressure (32 sccm DCM + 8 sccm N_2) in the SVA chamber as described previously.^{24,35} Note that the temperature of the DCM tank was kept at 20°C during the SVA process.

4.3 | Fabrication of DIS and GYR-structured PS-*b*-P2VP-*b*-PEO SPEs

To produce PS-*b*-P2VP-*b*-PEO SPEs, the DIS and GYR-structured films were first detached from their substrate by solubilizing the sacrificial PEDOT:PSS layer in a deionized water bath. The square-shaped PS-*b*-P2VP-*b*-PEO films were then infused by a 1 wt% LiIAC solution (300 mg of LiIAC in 30 g of deionized water) for different times (1 and 48 h in this study). Finally, the SPEs with a DIS or GYR phase were washed in a deionized water bath, cut into discs with a diameter of 2.5 cm, and wrapped in a wipe to remove the excess of water.

4.4 | Ionic conductivity and DMA measurements

The ionic conductivities of 25 μm thick SPEs with a DIS or GYR phase were recorded by using EIS (Solartron 1260 impedance analyzer) over a frequency range between 1 and 1000 Hz with an amplitude of 50 mV. For that purpose, the DIS and GYR-structured SPEs were placed into a sample holder (BioLogic CESH-e) with circular gold-plated blocking electrodes (2 cm diameter), and then compressed to allow through-plane measurements at different temperatures between 20 and 90°C. Prior to EIS measurements, samples were heated at 50°C for 1 h and, subsequently, equilibrated at 20°C to eliminate traces of water and to ensure a good interfacial contact with the electrodes. Thermomechanical properties (elastic storage modulus, E') of a 25 μm thick GYR-structured film were assessed using a DMA 242 E Artemis from NETZCH. The sample was heated from 25 to 200°C at a rate of 2°C min^{-1} , a frequency of 1 Hz and a displacement amplitude of 10 μm (0.1% of strain).

4.5 | AFM and SEM imaging

AFM (nano-observer, CSInstruments) was used in tapping mode to characterize the surface morphology of PS-*b*-P2VP-*b*-PEO films. Silicon cantilevers (PPP-NCH, Nanosensors) with a typical tip radius of ~ 5 nm were used. The resonance frequency of cantilevers was ~ 235 kHz. SEM (Hitachi S-4800) was used at an accelerating voltage of 5 kV to acquire top view and cross-section images of both DIS and GYR-structured films.

4.6 | GISAXS characterizations

GISAXS experiments were performed on an Anton Paar SAXSPPOINT 5.0 equipped with a PRIMUS copper X-ray source ($\lambda = 0.15418$ nm). The X-ray beam incident angle with respect to the sample surface was set at 0.4° , which is slightly larger than the critical angle of total external reflection of the polymer, ensuring full penetration of the X-ray beam in the material and hence, analyzing the full volume of the sample. The 2D scattering patterns were collected with a Dectris Eiger2 R 1M detector. The measuring geometry was calibrated with silver behenate as standard, and a sample-to-detector distance of 1300 mm was used. For each measurement 48 30-min frames were averaged.

4.7 | FTIR, XPS, and Raman measurements

FTIR spectra was monitored on a Thermo Nicolet Nexus FTIR spectrometer with a diamond ATR attachment, and samples were subjected to 32 scans in the range of 4000 and 650 cm^{-1} . XPS was performed on an ESCALAB 250 (Thermo Electron) with a monochromatic Al K α (1486.6 eV) source operating at 150 W (15 kV and 10 mA). The analyzed surface area was $500\text{ }\mu\text{m}^2$ with a sampling depth of ~ 5 nm. The emitted photoelectrons were detected perpendicular to the sample surface with a constant analyzer energy mode. Data analysis was carried out using the Advantage software. BEs of all core levels are referred to the C—C bond of C1s (at 284.8 eV). The charge is compensated by a low energy (-2 eV) electron beam. N1s and I3d high-resolution spectra were recorded at a step of 0.1 eV (transition energy of 20 eV). Micro-Raman analyses were conducted using a HORIBA Jobin LabRAM HR800UV Raman spectrometer ($\lambda = 660$ nm, 1800 gr mm^{-1} grating) with a Leica PL Fluotar $\times 50$ objective (NA = 0.55). Si vibration at 520 cm^{-1} was employed for calibration. Raman spectra were typically collected with 60 s exposure time and four accumulations

at a laser power of 10 mW. No post-processing was performed on obtained data.

ACKNOWLEDGMENTS

This work was performed within the support of the ANR JCJC AFM_Ring project, grant ANR-18-CE09-00xx of the French Agence Nationale de la Recherche. The authors also thank the Balard Analysis and Characterizations Plateform (UAR 2041 PAC Chimie Balard Montpellier) facilities for technical support.

ORCID

Karim Aissou  <https://orcid.org/0000-0002-9236-464X>

REFERENCES

- [1] Y. Zheng, Y. Yao, J. Ou, M. Li, D. Luo, H. Dou, Z. Li, K. Amine, A. Yu, Z. Chen, *Chem. Soc. Rev.* **2020**, *49*, 8790.
- [2] B. Dunn, H. Kamath, J.-M. Tarascon, *Science* **2011**, *334*, 928.
- [3] G. Zubi, R. Dufo-López, M. Carvalho, G. Pasaoglu, *Renewable Sustainable Energy Rev.* **2018**, *89*, 292.
- [4] J. Wan, J. Xie, X. Kong, Z. Liu, K. Liu, F. Shi, A. Pei, H. Chen, W. Chen, J. Chen, X. Zhang, L. Zong, J. Wang, L.-Q. Chen, J. Qin, Y. Cui, *Nat. Nanotechnol.* **2019**, *14*, 705.
- [5] X.-B. Cheng, R. Zhang, C.-Z. Zhao, Q. Zhang, *Chem. Rev.* **2017**, *117*, 10403.
- [6] W. Ren, Y. Zheng, Z. Cui, Y. Tao, B. Li, W. Wang, *Energy Storage Mater.* **2021**, *35*, 157.
- [7] H. Adenusi, G. A. Chass, S. Passerini, K. V. Tian, G. Chen, *Adv. Energy Mater.* **2023**, *13*, 2203307.
- [8] E. Quartarone, P. Mustarelli, A. Magistris, *Solid State Ionics* **1998**, *110*, 1.
- [9] W. Young, T. H. Epps, *Macromolecules* **2009**, *42*, 2672.
- [10] W.-S. Young, W.-F. Kuan, T. H. Epps, *J. Polym. Sci. Part B: Polym. Phys.* **2014**, *52*, 1.
- [11] H. N. Wang, T. Y. Hou, H. Cheng, B. W. Jiang, H. H. Xu, Y. H. Huang, *J. Energy Chem.* **2022**, *71*, 218.
- [12] M. Takahashi, T. Watanabe, K. Yamamoto, K. Ohara, A. Sakuda, T. Kimura, S. Yang, K. Nakanishi, T. Uchiyama, M. Kimura, A. Hayashi, M. Tatsumisago, Y. Uchimoto, *Chem. Mater.* **2021**, *33*, 4907.
- [13] P. P. Soo, B. Huang, Y. I. Jang, Y. M. Chiang, D. R. Sadoway, A. M. Mayes, *J. Electrochem. Soc.* **1999**, *146*, 32.
- [14] M. Singh, O. Odusanya, G. M. Wilmes, H. B. Eitouni, E. D. Gomez, A. J. Patel, V. L. Chen, M. J. Park, P. Fragouli, H. Iatrou, N. Hadjichristidis, D. Cookson, N. P. Balsara, *Macromolecules* **2007**, *40*, 4578.
- [15] L. Yan, C. Rank, S. Mecking, K. I. Winey, *J. Am. Chem. Soc.* **2020**, *142*, 857.
- [16] J. Park, K. I. Winey, *JACS Au* **2022**, *2*, 1769.
- [17] T. Niitani, M. Shimada, K. Kawamura, K. Dokko, Y.-H. Rho, K. Kanamura, *Electrochem. Solid-State Lett.* **2005**, *8*, A385.
- [18] P. Sutton, P. Bennington, S. N. Patel, M. Stefik, U. B. Wiesner, P. F. Nealey, U. Steiner, I. Gunkel, *Adv. Funct. Mater.* **2019**, *29*, 1905977.
- [19] J.-H. Choi, Y. Ye, Y. A. Elabd, K. I. Winey, *Macromolecules* **2013**, *46*, 5290.

- [20] N. Byrne, P. C. Howlett, D. R. MacFarlane, M. Forsyth, *Adv. Mater.* **2005**, *17*, 2497.
- [21] N. Byrne, P. C. Howlett, D. R. MacFarlane, M. E. Smith, A. Howes, A. F. Hollenkamp, T. Bastow, P. Hale, M. Forsyth, *J. Power Sources* **2008**, *184*, 288.
- [22] M. Irfan, Y. Zhang, Z. Yang, J. Su, W. Zhang, *J. Mater. Chem. A* **2021**, *9*, 22878.
- [23] S. D. Jones, H. Nguyen, P. M. Richardson, Y. Q. Chen, K. E. Wyckoff, C. J. Hawker, R. J. Clément, G. H. Fredrickson, R. A. Segalman, *ACS Cent. Sci.* **2022**, *8*, 169.
- [24] K. Aissou, H. Bouzit, F. Krusch, J.-P. Méricq, D. Cot, N. Masquelez, S. Roualdes, D. Quémener, *Macromol. Rapid Commun.* **2022**, *43*, 2100585.
- [25] C. G. Arges, Y. Kambe, H. S. Suh, L. E. Ocola, P. F. Nealey, *Chem. Mater.* **2016**, *28*, 1377.
- [26] C.-C. Yang, P. Puneet, I.-M. Lin, Y.-W. Chiang, R.-M. Ho, *Giant* **2021**, *7*, 100059.
- [27] L. He, L. Chen, X. Dong, S. Zhang, M. Zhang, X. Dai, X. Liu, P. Lin, K. Li, C. Chen, T. Pan, F. Ma, J. Chen, M. Yuan, Y. Zhang, L. Chen, R. Zhou, Y. Han, Z. Chai, S. Wang, *Chem* **2021**, *7*, 699.
- [28] T. W. Kang, J. H. Lee, J. Lee, J. H. Park, J. H. Shin, J. M. Ju, H. Lee, S. U. Lee, J.-H. Kim, *Adv. Mater.* **2023**, *35*, 2301308.
- [29] I. Jerman, V. Jovanovski, A. S. Vuk, S. B. Hocevar, M. Gaberscek, A. Jesih, B. Orel, *Electrochim. Acta* **2008**, *53*, 2281.
- [30] P. Deplano, J. R. Ferraro, M. L. Mercuri, E. F. Trogu, *Coord. Chem. Rev.* **1999**, *188*, 71.
- [31] A. Spadoni, M. Falconieri, M. Lanchi, R. Liberatore, M. Marrocco, G. S. Sau, P. Tarquini, *Int. J. Hydrogen Energy* **2012**, *37*, 1326.
- [32] P. Braun, C. Uhlmann, A. Weber, H. Störmer, D. Gerthsen, E. Ivers-Tiffée, *J. Electroceramics* **2017**, *38*, 157.
- [33] S. Zekoll, C. Marriner-Edwards, A. K. O. Hekselman, J. Kasemchainan, C. Kuss, D. E. J. Armstrong, D. Cai, R. J. Wallace, F. H. Richter, J. H. J. Thijssen, P. G. Bruce, *Energy Environ. Sci.* **2018**, *11*, 185.
- [34] G. Lingua, P. Grysan, P. S. Vlasov, P. Verge, A. S. Shaplov, C. Gerbaldi, *Macromolecules* **2021**, *54*, 6911.
- [35] K. Aissou, M. Coronas, D. Hermida-Merino, E. Solano, D. Cot, S. Roualdes, D. Bouyer, D. Quemener, *Int. J. Polym. Sci.* **2023**, *2023*, 1.

SUPPORTING INFORMATION

Additional supporting information can be found online in the Supporting Information section at the end of this article.

How to cite this article: K. Aissou, M. Coronas, J. Richard, C. Bakkali-Hassani, S. Vishwakarma, E. Petit, A. van der Lee, S. Roualdes, *J. Polym. Sci.* **2024**, *62*(20), 4567. <https://doi.org/10.1002/pol.20240206>